Fundamental parameters of the massive eclipsing binary HM1 8⋆

C. N. Rodríguez[1,2]†, G. A. Ferrero[1,2], O. G. Benvenuto[1,2]‡, R. Gamen[1,2], N. I. Morrell[3], R. H. Barbá[4], J. Arias[4] and P. Massey[5,6]

[1]*Instituto de Astrofísica de La Plata, IALP, CCT-CONICET-UNLP, Argentina*
[2]*Facultad de Ciencias Astronómicas y Geofísicas, Universidad Nacional de La Plata, Paseo del Bosque S/N, B1900FWA La Plata, Argentina.*
[3]*Las Campanas Observatory, Carnegie Observatories, Casilla 601, La Serena, Chile.*
[4]*Departamento de Astronomía, Universidad de La Serena, Cisternas 1200 Norte, La Serena, Chile.*
[5]*Lowell Observatory, 1400 W Mars Hill Road, Flagstaff, AZ 86001, USA.*
[6]*Department of Astronomy and Planetary Science, Northern Arizona University, Flagstaff, AZ 86001-6010, USA.*

Accepted XXX. Received YYY; in original form ZZZ

ABSTRACT

We present a comprehensive study of the massive binary system HM1 8, based on multi-epoch high resolution spectroscopy, V-band photometry and archival X-ray data. Spectra from the *OWN Survey*, a high resolution optical monitoring of Southern O and WN stars, are used to analyse the spectral morphology and perform quantitative spectroscopic analysis of both stellar components. The primary and secondary components are classified as O4.5 IV(f) and O9.7 V, respectively. From a radial-velocity (RV) study we derived a set of orbital parameters for the system. We found an eccentric orbit ($e = 0.14 \pm 0.01$) with a period of $P = 5.87820 \pm 0.00008$ days. Through the simultaneous analysis of the RVs and the V-band light curve we derived an orbital inclination of $70.0° \pm 2.0$ and stellar masses of $M_a = 33.6^{+1.4}_{-1.2}$ M$_\odot$ for the primary, and $M_b = 17.7^{+0.5}_{-0.7}$ M$_\odot$ for the secondary. The components show projected rotational velocities $v_1 \sin i = 105 \pm 14$ km s^{-1} and $v_2 \sin i = 82 \pm 15$ km s^{-1}, respectively. A tidal evolution analysis is also performed and found to be in agreement with the orbital characteristics. Finally, the available X-ray observations show no evidence of a colliding winds region, therefore the X-ray emission is attributed to stellar winds.

Key words: stars: early-type – stars: fundamental parameters – stars: individual: HM1 8 – binaries: close – binaries: eclipsing

1 INTRODUCTION

Massive stars are those that end their lives as core-collapse supernovae, creating neutron stars or black holes. They play a key role in the astrophysics of their host galaxy due to their ionising UV fluxes, powerful winds and extreme stellar properties (Zinnecker & Yorke 2007). Usually found in star forming regions, they are excellent tracers of recent star formation, as their input dominate the total luminosity of the environment (Massey 2003). They also contribute to the chemical evolution of their host galaxy by means of their stellar winds and supernovae explosions (Maeder 1998; Langer 2012 and references therein). From a spectroscopic point of view, massive stars are found as main sequence O and early B types, and later as Wolf-Rayet (WR) stars and red supergiants, which evolve to their explosive end in a few million years or less. In spite of their importance, our knowledge on some properties of these stars, such as their formation mechanisms and their masses, is still incomplete.

Massive stars show a high degree of multiplicity. In the Milky Way, at least 70% of the O-type stars are found in binaries and multiple systems (Barbá et al. 2017; Sana et al. 2012). Detailed studies of multiple stars allow derivation of important physical parameters, such as absolute masses and radii. Different scenarios have been proposed for the formation of massive stars (Zinnecker & Yorke 2007), although none of them entirely explains the precise forming mechanism; the orbital parameters of multiple systems can provide information on enviromental conditions during star formation (Mahy et al. 2013). Although the evolution of massive stars is mainly determined by initial masses and mass-loss rates (Chiosi & Maeder 1986), multiplicity may affect the evolutionary path of the components in short-period systems (Sana & Evans 2010; Langer 2012; Mahy et al. 2013).

Since the era of *Einstein* X-ray telescope, it is known that massive stars earlier than mid-B emit X-rays (Harnden et al. 1979). Their origin is still debated but the most accepted models attribute this emission to plasma heated by shocks formed from intrinsic instabilities associated with radiatively-driven stellar winds (e.g. Lucy & White 1980; Owocki et al. 1988; Feldmeier et al. 1997; Owocki et al. 2013). The X-ray luminosity is therefore expected to correlate with stellar parameters (Sciortino et al. 1990; Nebot Gómez-Morán & Oskinova 2018). In particular, it has been found that the X-ray luminosity (L_X) of O-type stars linearly scales with their bolometric luminosities (L_{BOL}) (Nebot Gómez-Morán & Oskinova 2018 and references therein). Then, if the ratio L_X/L_{BOL} can be obtained from observations, it could be inferred where the X-ray radiation comes

⋆ This paper includes data obtained with the 6.5 m Magellan Telescopes located at Las Campanas Observatory, Chile.
† E-mail: cnrodriguez@fcaglp.unlp.edu.ar
‡ Member of the Carrera del Investigador Científico, Comisión de Investigaciones Científicas de la Provincia de Buenos Aires (CIC).

Table 1. Technical characteristics of the spectrographs used for this work.

Observatory	Telescope	Spectrograph	Spectral range [Å]	Resolving power
Las Campanas	Irénée du Pont (2.5 m)	Echelle	~ 3600 – 10100	~ 20 000
La Silla	MPG/ESO (2.2 m)	FEROS	~ 3600 – 9200	~ 48 000
Las Campanas	Clay-Magellan (6.5 m)	MIKE	~ 3200 – 5000 (blue)	~ 28 000
			~ 4900 – 10000 (red)	~ 22 000

from (if the star is actually emitting it or a colliding-wind region exists), and help us constrain the astrophysical models.

In this work we concentrate on HM1 8 (HM1 VB10; $\alpha = 17^{\rm h}\,19^{\rm m}\,04\overset{\rm s}{.}4$, $\delta = -38^\circ\,49'\,05''$), a member of the open cluster Havlen & Moffat No. 1 (HM1 = C 1715-387; $l = 348.7^\circ$, $b = -0.8^\circ$). This is a compact group of stars situated in the inner part of our Galaxy, beyond the Sagittarius arm ($V_0 - M_V = 12.6$ or $d = 3.3$ kpc), and highly reddened ($E_{B-V} = 1.84 \pm 0.07$ mag) according to Vázquez & Baume (2001). HM1 8 was firstly classified as an O8 star by Havlen & Moffat (1977), and subsequently reclassified as O5 V (Massey et al. 2001), and O5 III(f) (Gamen et al. 2008; Sota et al. 2014). Its binary nature was discovered by Gamen et al. (2008) who found an orbital period of 5.9 days and minimum masses of 31 $M_\odot$ and 15 $M_\odot$, suggesting the secondary component is also an OB star. In the X-ray domain, Nazé et al. (2013) used data from the *XMM-Newton* satellite to study and characterize the properties of the stars in HM1, including HM1 8.

The goal of this work is to enlarge and deepen the study of HM1 8. The structure of the paper is as follows: the observations are described in Sec. 2; sections 3 and 5 present the optical spectroscopic and photometric studies of the system; an up-to-date X-ray study of HM1 8 is included in section 6, and the tidal evolution of the pair is discussed in section 7. Finally, results and some conclusions are summarized in Sec. 8.

2 OBSERVATIONS

The data considered in this study comprise three categories: optical spectroscopy, optical photometry, and X-ray archival observations. Observations were carried out at different facilities as explained in the following sections.

2.1 Optical spectroscopy

The spectroscopic data used in this work were obtained under the OWN Survey project between 2006 and 2014. This is a high resolution optical spectroscopic survey of a large sample (≈ 300 stars) of Southern O and WN stars for which no multiplicity indication was available at the beginning of the project (Gamen et al. 2008; Barbá et al. 2017). In this case, the spectra were obtained with three spectrographs available at two different observatories in Chile: these are the échelle spectrograph attached to the 2.5 m du Pont telescope, the Magellan Inamori Kyocera Echelle (MIKE) at the 6 m Magellan Clay telescope, both at Las Campanas Observatory, and the Fibre-fed optical echelle spectrograph (FEROS), at the 2.2 m telescope at La Silla Observatory. Table 1 summarises the main properties of each instrumental configuration. Spectra from Las Campanas Observatory were reduced using the standard IRAF[1] routines; in the case of du Pont a 2×2 binning was applied to the CCD. FEROS spectra were reduced with the standard reduction pipeline in the MIDAS package provided by the European Southern Observatory (ESO). Typical exposure times were from 30 to 40 minutes, which provided spectra with signal-to-noise ratios (SNR) ranging from 30 in the blue to 100 in the yellow-red region of the spectrum.

2.2 Optical photometry

Photometric observations were obtained during a monitoring of stars in OB associations looking for eclipsing massive binaries (Massey et al. 2012). The observations used in this work were obtained in the V filter, with exposure times of 10-30 s typically. The data were collected with two different telescopes: the 1.0 m Yale telescope at Cerro Tololo Interamerican Observatory, operated by SMARTS, and the 1 m Swope telescope at Las Campanas Observatory. Table 2 summarises the principal characteristics of each instrumental setup. The data were reduced and measured by P.M. (SMARTS dataset) and R.G. (Swope dataset). The reader is referred to Massey et al. (2012) for details on the reduction procedure. The combined dataset includes a total of 924 V measurements, with typical errors of about 0.007 mag., which are presented in Table 3.

2.3 X-ray data

HM1 was observed on 2010 March 10 by the *XMM-Newton* X-ray satellite during the revolution 1877 (Obs-Id. 0600080101) for 25 ks. The observation, centred on $(\alpha, \delta)_{J2000}$= ($17^{\rm h}\ 19^{\rm m}\ 00\overset{\rm s}{.}48$, $-38^\circ\ 48'\ 00\overset{''}{.}5$), was acquired by the European Photon Imaging Camera (EPIC). This instrument consists of three detectors, two Metal Oxide Semiconductor (MOS) cameras (Turner et al. 2001), and one pn camera[2] (Strueder et al. 2000) operating in the 0.2-15 KeV range. The data were taken with the medium filter in full-frame mode. The reduction and analysis were carried out with the XMM Science Analysis System (SAS) version 15.0.0, following the threads recommended by the *XMM-Newton* team[3]. No background flare affected the observations, and no source is bright enough to suffer from pile-up. The latest calibrations were applied with the EMMPROC and EPPROC tasks. The events were filtered to retain only the patterns and photon energies likely for X-ray events: patterns 0-4 and energies 0.5 to 15 KeV for pn, and patterns 0-12 and energies from 0.5 to 10 KeV for MOS1/2

[1] IRAF was distributed by the National Optical Astronomy Observatory, which was operated by the Associated Universities for Research in Astronomy, Inc., under cooperative agreement with the National Science Foundation.
[2] The pn camera is a fully depleted, back illuminated detector with a p^+ back diode and a n^+ anode.
[3] Available at https://www.cosmos.esa.int/web/xmm-newton/sas-threads.

Table 2. Characteristics of telescopes and instruments used for photometric observations of HM1 8.

Observatory	Telescope	Camera	Scale [arcsec pix^{-1}]	FOV [arcmin]	Median seeing [arcsec]
Las Campanas	Swope (1 m)	SITe3	0.435	15×23	1.60
Cerro Tololo	SMARTS Yale (1 m)	Y4KCam	0.289	20×20	1.67

Table 3. V-band photometric data of HM1 8 used in this work. The full table with the 924 measurements and errors is available online as supplementary material.

HJD−2 400 000	V	σ_V	Telescope
53 134.7247	12.526	0.001	Swope
53 134.7353	12.533	0.003	Swope
53 134.7382	12.513	0.011	Swope
...	...	...	...

instruments. After this, we obtained clean event lists (calibrated and filtered) which will be used in the subsequent analysis.

3 SPECTRAL ANALYSIS

3.1 Radial velocity measurements

The high-resolution spectrum of HM1 8 reveals the double-lined spectroscopic nature of the system. Given the difference in the spectral types of the stellar components, not all of the absorption lines show contribution from both stars. To obtain the radial velocity (RV) measurements for the binary components, we adjusted a Gaussian function to the cores of selected spectral lines using the `splot` task of IRAF. The measured lines were He I λ5876, He II λ5412, He II λ4542, C III λ5696, C IV λ5812 for the primary, and He I λ5876 for the secondary. In the case of He I λ5876, we used two Gaussian functions to fit the profiles of both components simultaneously. The remaining lines were fitted using a single Gaussian function. The individual heliocentric RV measurements are listed in Table 4. Air wavelengths were taken from NIST Atomic Spectra Database Lines Form (Kramida et al. 2020), for He I λ5876, C III λ5696 and C IV λ5812 lines, and from Striganov & Sventitskii (1968), for the He II lines.

3.2 Spectral disentangling

The RV measurements above described provide a starting point to apply a spectral disentangling method in order to obtain the individual spectra of each system's component. In this case, we implemented the method developed by González & Levato (2006), following the procedure applied by Barbá et al. (2020) in the analysis of the O+O system HD 54662 AB. Compared to HD 54662 AB, HM1 8 has the advantage of presenting orbital phases for which the spectral lines of the components are clearly separated, and the profiles are not blended at all (e.g. He I λ5876). To start the process we used FASTWIND models as initial templates, corresponding to $T_{\rm eff}$ of 41 000 K and 33 000, for the primary and secondary, respectively, and $\log g = 4.0$ for both components. Initial values for the projected rotational velocities ($v \sin i$) were estimated from the Gaussian fitting of the corresponding He I λ5876 profiles. The methodology used to obtain FASTWIND models is presented in Section 3.5. The disentangling process converged very well after about 20 iterations. The convergence was greatly improved by centering the cross-correlation process in a few strong lines: He II λ4542, He II λ5412, O III λ5592, C IV λ5812, He I λ5876 and He II λ6683 for the primary, and He I λ4922, He I λ5876 and He I λ6678 for the secondary component. The final disentangled spectra for both components of the system (component A and component B templates) are obtained from the combination of ten spectra with good SNR obtained at or near the orbital quadratures. Both templates are shown in Fig 1, along with a composite spectrum obtained as the sum of four spectra at the upper quadrature of the primary component. The resulting individual spectra were used to determine the RVs of spectra not included in the disentangling process, applying a similar iterative method: RVs of each component are determined iteratively via cross-correlation (using IRAF FXCOR) after subtraction of the template of the companion star shifted to the appropriate RV. The convergence is reached after a few iterations. The final RV measurements and their errors are listed in Table 4. The comparison of these values with the RV measurements obtained using Gaussian fitting shows very consistent results and the RVs obtained through cross-correlation delivered the best spectroscopic orbital solution (see Section 4).

Two characteristics of the disentangled spectra which arise in the large reddening that affects this star must be mentioned. First, the SNR is not uniform along the covered spectral range. For example the SNR in the blue (λ4600 Å) is about 30 for most spectra; thus, as the secondary contributes with about 20% of the total light (see Section 3.5) the SNR of its spectra is lower than 10. With this situation, small differences in the continuum normalization could affect the disentangling result. In the next subsection we compare the template B with standard stars for spectroscopic classification as a proof of the reliability of our methodology. A second characteristic is the large number of strong and broad diffuse interstellar bands (DIBs) distributed along the spectrum, mostly in the yellow-red portion. These DIBs were not removed before the disentangling process, producing a wobbly appeareance of the continuum or structured profiles in some DIBs (e.g. λ5870). Fortunately, these DIBs did not affect the main lines used for spectral classification and RV determinations.

3.3 Spectral classification

The spectral classification of both components was performed based on the templates obtained from the disentangling method, verifying that all the spectral lines were present in the original composite spectrum in quadrature. We followed the schema presented by Sota et al. (2011) (updated in Maíz Apellániz et al. 2016) in *The Galactic O-star Spectroscopic Survey* (GOSSS). The template spectra were resampled to mimic the resolving power of GOSSS spectra, i.e. $R \approx 2500$.

The spectrum of the primary component presents the He I λ4471 line considerably weaker than the He II λ4542 line. A detailed comparison with the standard stars HD 93843 and HD 193682, corresponding to the types O5 III and O4.5 IV, respectively, shows that the primary is closer to HD 193682 (see Figure 2). Additionally, the strength of the N III λ4634/41/42 emissions and the almost filled He II

Table 4. Radial velocity measurements (in km s^{-1}) for the stellar components of HM1 8. The label "a" and "b" indicates primary and secondary components, respectively. RV values determined near conjuntions (marked with ∗) were not used in the orbital solution.

HJD	He I λ5876		He II λ5412	He II λ4542	C III λ5696	C IV λ5812	C ross-correlation		Instrument
2400000+	5875.62 Å		5411.52 Å	4541.59 Å	5695.92 Å	5811.98 Å			
	a	b	a	a	a	a	a	b	
53873.858	93.5	-227.0	107.0	65.4	89.3	95.4	90.8	-213.4	du Pont echelle
53874.870	109.4	-255.4	121.4	154.0	102.5	113.0	106.6	-245.1	du Pont echelle
53877.785	-100.5	-	-99.7	-77.5	-109.2	-108.4	-115.1	172.8	du Pont echelle
53920.751	78.7	-209.0	91.1	90.3	79.4	77.1	73.6	-203.0	du Pont echelle
53921.734	116.6	-275.3	137.2	126.2	122.7	112.8	112.7	-262.7	du Pont echelle
53937.635	-17.5	-	10.5	13.4	13.6	-5.6	−2.5*	−41.6*	du Pont echelle
53938.710	100.3	-264.0	111.9	117.8	105.1	108.9	97.6	-247.0	du Pont echelle
53954.570	-48.7	-	-51.7	-54.4	-76.4	-69.1	-75.1	100.4	MIKE
53954.586	-41.6	-	-45.7	-46.5	-63.2	-61.9	-72.0	88.7	MIKE
53955.588	22.4	-	-	-	47.0	66.2	25*	-	MIKE
53987.508	-36.6	-	-39.2	-25.8	-67.4	-61.0	−17*	-	du Pont echelle
53988.504	-157.6	264.9	-157.3	-150.0	-158.0	-170.9	-167.4	282.0	du Pont echelle
53989.517	-95.4	159.7	-81.4	-86.0	-92.3	-99.8	-104.5	174.9	du Pont echelle
53990.520	-13.3	-	17.1	51.3	20.8	-1.8	−0.7*	−50.7*	du Pont echelle
53991.527	110.6	-242.0	101.3	107.3	148.5	158.4	99.6	-236.3	du Pont echelle
54198.868	-18.5	-	3.5	23.9	-17.7	-35.3	−2.5*	−58.4*	du Pont echelle
54257.750	-11.9	-	-10.1	-	-13.0	-32.3	−7.1*	−51.4*	du Pont echelle
54258.805	-172.7	267.1	-159.8	-149.7	-172.1	-165.1	-163.7	263.8	du Pont echelle
54600.726	-123.5	176.0	-110.5	-111.6	-121.1	-122.8	-129.6	183.4	FEROS
54626.784	120.4	-282.7	141.6	115.5	110.5	127.4	112.4	-261.6	FEROS
54953.803	-73.0	-	-65.0	-63.4	-78.9	-79.4	-88.4	108.6	FEROS
54956.807	80.1	-203.6	80.7	85.8	73.2	79.9	74.8	-194.0	FEROS
54961.793	113.4	-293.8	131.0	142.8	107.0	117.0	105.9	-272.1	du Pont echelle
54964.682	-164.7	273.1	-138.2	-147.3	-153.5	-165.1	-179.0	271.0	du Pont echelle
54976.747	-139.8	207.1	-126.0	-131.4	-135.3	-135.7	-149.0	218.9	FEROS
56813.780	115.4	-261.6	143.1	117.2	118.4	120.3	109.8	-251.7	du Pont echelle
56815.818	-150.4	253.7	129.3	-135.3	-152.0	-156.7	-158.7	262.2	du Pont echelle

λ4686 absorption indicate the (f) qualifier. Thus, we classified the primary star of HM1 8 as O4.5 IV(f)[4].

In the spectrum of the secondary component of HM1 8, we identified He I $\lambda\lambda$4388, 4471, and 4713, He II λ4686, weak He II λ4542 and Si III λ4553 absorption lines, indicating a late-O or early-B spectral type. Besides, the relative strengths of He II λ4686 and He I λ4713 point to luminosity class V. In Fig. 3, we plot the spectrum of HM1 8b along with the GOSSS (Maíz Apellániz et al. 2016) classification standards AE Aur (O9.5 V), υ Ori (O9.7 V); and the Sota et al. (2011) standards τ Sco (B0 V) and HD 2083 (B0.2 V). Based on the strength of He II λ4542 compared to Si III λ4553, it can be seen that HM1 8b more closely resembles υ Ori than τ Sco, a conclusion also supported by the relative strengths of He II λ4686 and He I λ4471. Thus, we classified this component as O9.7 V.

3.4 Spectral line-broadening analysis

A spectral line-broadening analysis of the spectra was performed in order to study the rotational velocity of each star, as well as to identify other possible macro-broadening mechanisms. We used the IACOB-BROAD tool (Simón-Díaz & Herrero 2014), which characterises the line-broadening of OB-type stars using a combined Fourier Transform (FT) and Goodness-Of-Fit (GOF) methodology. IACOB-BROAD allows the user to estimate the projected rotational velocity ($v \sin i$) and the macroturbulence broadening ($v_{\rm mac}$) of the stars from the high resolution spectra. According to Simón-Díaz & Herrero (2007), metallic absorption lines are more suitable for this analysis since they are less affected by other broadening effects besides rotation. Hence, we considered the C IV λ5812 line for the primary component, but for the secondary there was no metal line appropriate for this analysis, for what we considered He I λ5875.

The analysis was performed using both the disentangled templates, a composite of 3 observed spectra and a FEROS spectrum at the orbital quadrature. As we are working with the templates and an observed composite spectrum, and the tool contemplates individual stars, we needed to correct it by their respective dilution factors. We estimated them from their calibrated magnitudes (according to their spectral types), understanding the dilution factor as an estimation of the fraction of observed flux from the spectra that corresponds to a specific component (we estimated dilution factors of 0.8 and 0.2 for the primary and secondary component, respectively). As will be shown below, these dilution factors permit comparison of the templates with the determined models accordingly.

The best fits obtained in this analysis were obtained with the observed composite spectrum and they are shown in Fig. 4. For the primary star we found $v \sin i = 105 \pm 14$ km s^{-1} and $v_{\rm mac} = 67 \pm 6$ km s^{-1}. The macroturbulence velocity, which represents all causes of macro-broadening other than rotation, is significant for this component. This points to the existence of extra broadening mechanisms of different physical origins, for example, cyclic surface motions initiated by turbulent pressure instabilities (Simón-Díaz et al. 2017).

[4] It is worth to note that the profile of He II λ4686 is similar to that of HD 93843, suggesting a luminosity class III. However, as the O4 III spectral class does not have an assigned standard yet, we do not extrapolate following rigorously the Morgan-Keenan (MK) spectral classification process.

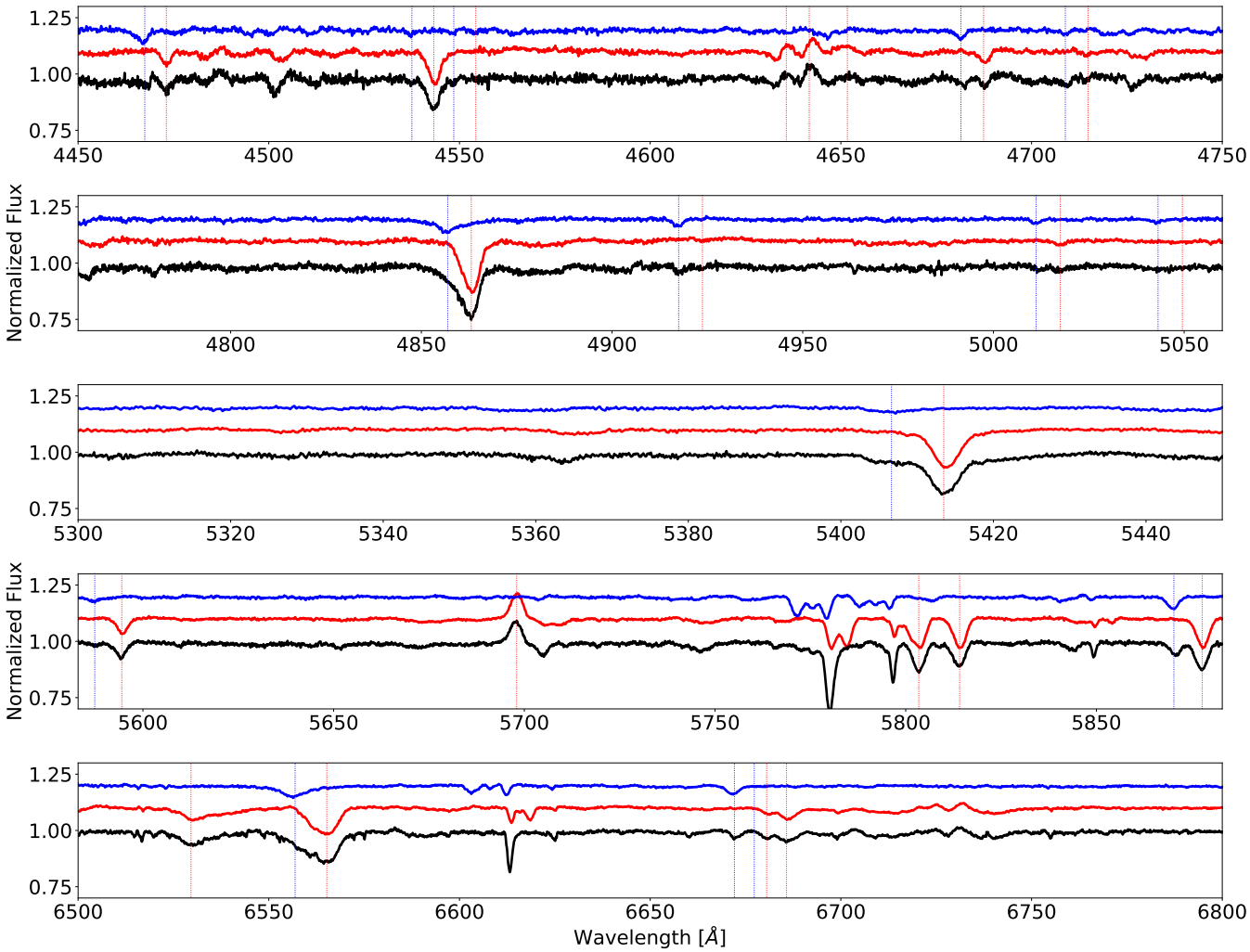

Figure 1. Templates obtained from the disentangling method (primary in red and secondary in blue), compared with a composite spectrum generated by combining the best four spectra during the upper quadrature of the primary star. In each panel, we draw vertical lines depicting the (shifted) wavelengths for the primary (in red) and secondary (in blue) components of most important spectral features: He I λ4471, He II λ4542, Si III λ4553, N III λ4634/41, C III λ4651, He II λ4686, He I λ4713, H$_\beta$, He I λ4922, He I λ5016, He I λ5047, He II λ5412, O III λ5592, C III λ5696, C IV λ5801-12, He I λ5876, He II λ6527, H$_\alpha$, He I λ6678, and He II λ6683.

The derived values for the secondary are $v \sin i$ = 82 ± 15 km s^{-1} and $v_{\rm mac}$ = 22 ± 7 km s^{-1}, meaning that the broadening is fully dominated by rotation.

3.5 Quantitative analysis

We carried out a quantitative analysis of the system's components to estimate their atmospheric parameters: effective temperature $T_{\rm eff}$, surface gravity log g and wind strength Q (where $Q = \dot{M}/(v_\infty R)^{1.5}$, being v_∞ the wind terminal velocity).

We employed the IACOB Grid-Based Automatic Tool (IACOB-GBAT), which is an IDL package that compares the observed spectrum with a large grid of FASTWIND models (Puls et al. 2005; Santolaya-Rey et al. 1997), convolved with their corresponding $v \sin i$ and $v_{\rm mac}$, and selects the one with the best fit (by means of a χ^2 algorithm). In this way, IACOB-GBAT performs a quantitative spectroscopic analysis based on standard techniques for O stars, using optical H and He lines (Simón-Díaz et al. 2011).

We run IACOB-GBAT on the template of HM1-8a using, as input parameters, $T_{\rm eff}$ and log g values for an O5 III star (Martins et al. 2005). We also adopted the broadening parameters found previously using the IACOB-BROAD tool, and fixing the associated helium abundances (Y$_{\rm He}$=0.10), the microturbulent velocities (ξ_1=5 km s^{-1}), and the wind parameter β=0.8. We fitted the following lines: Hα, Hβ, and Hγ; He I λ4471 and 5876; and He II λ4542 and 5412. The obtained parameters are shown in Table 5 and the comparison with the model is depicted in Fig. 5. The overall agreement between the FASTWIND model and the disentangled spectrum for the primary component is fairly good. A wind component (log Q = −12.3) is needed in order to fit the He II λ4686 and Hα profiles.

For HM1-8b, we also ran IACOB-GBAT on its disentangled spectrum, providing as input parameters $T_{\rm eff}$ and log g values for an O9.5 V star (Martins et al. 2005). The broadening parameters were adopted from the analysis with IACOB-BROAD. The fitted lines were: Hα, Hβ, Hγ, He I λ4471, 4713, 4922, 5015 and 5876; and He II λ4542, 4686 and 5411. The parameters were derived with log g = 4.0 fixed, and are

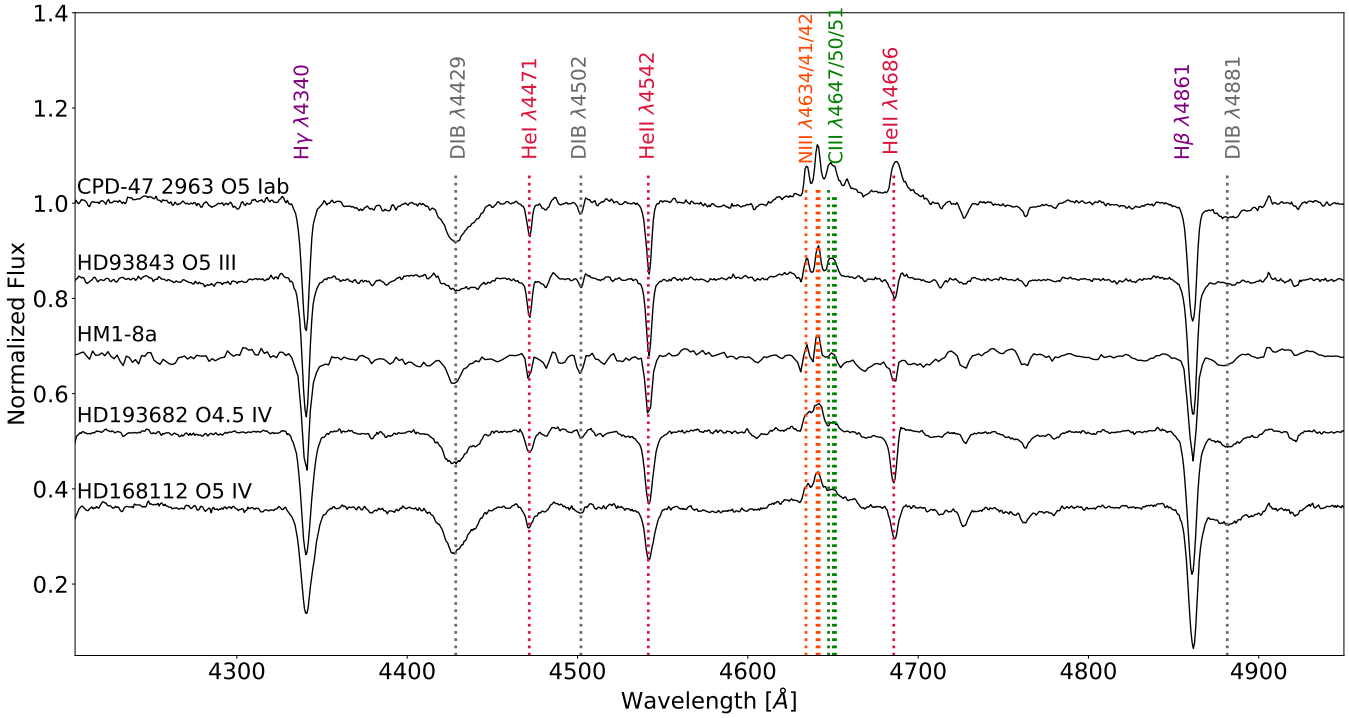

Figure 2. Comparison of the spectrum of HM1 8a with the standards defined by Maíz Apellániz et al. (2016).

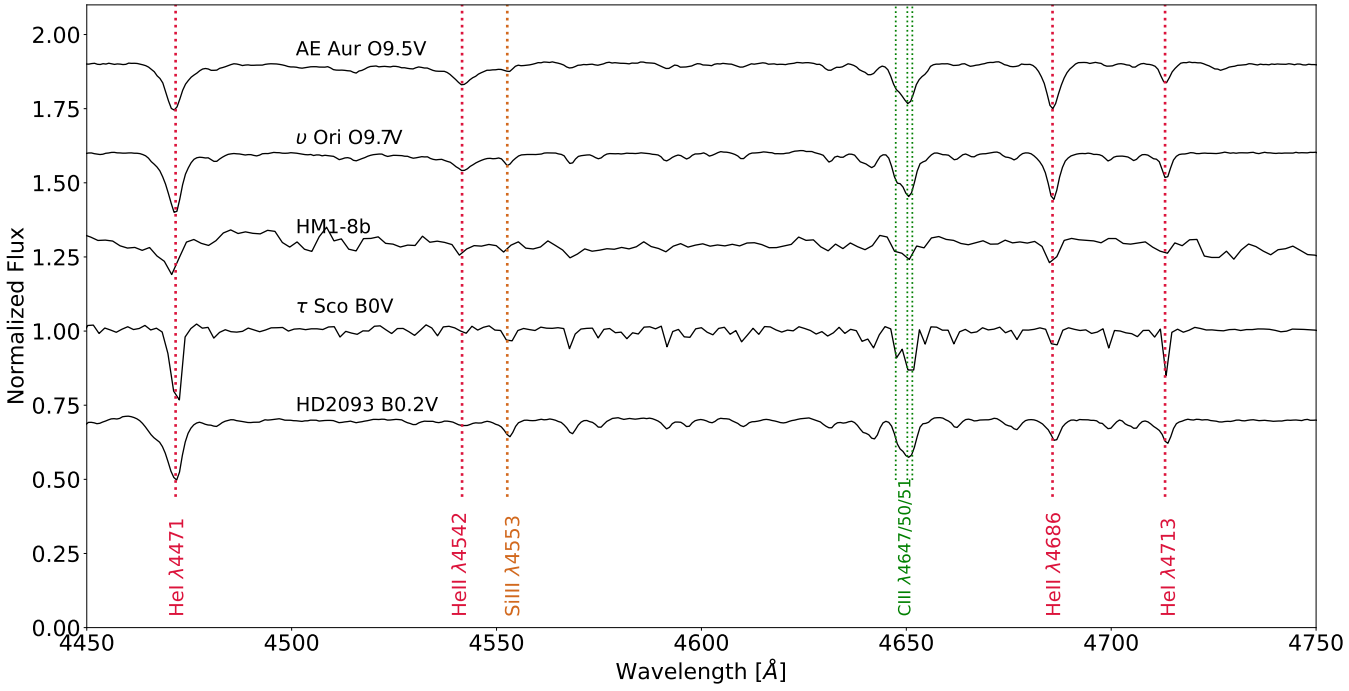

Figure 3. Comparison between the template of the secondary component (HM1 8b) and the spectroscopic standards for O9.5 V, O9.7 V, B0 V, and B0.2 V spectral types.

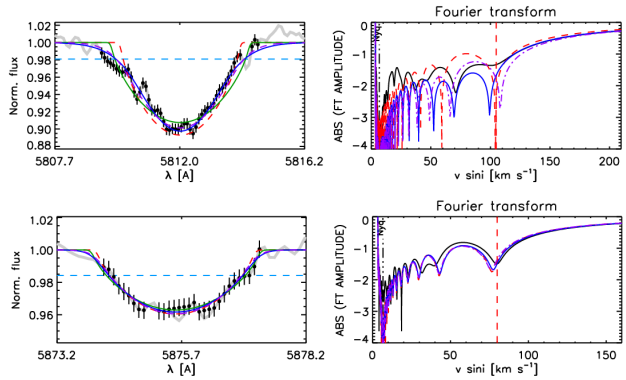

Figure 4. Characterisation of line-broadening of HM1 8 primary (top) and secondary (bottom) components obtained with the IACOB-BROAD tool. Left: C IV λ5812 of the primary and He I λ5875 for the secondary in the composite spectrum (black line) with superimposed: Fourier Transform (FT) fit (red), Goodness-Of-Fit (GOF) (blue), GOF without considering macroturbulence (green), and GOF taking into account the projected rotational velocity from the FT (purple). Horizontal dashed light blue line: estimated level of noise. Right: FT for the different methods, showing the first minimum (vertical dashed red line), where the projected rotational velocity is calculated (colours as in left panel).

Table 5. Parameters obtained from the quantitative spectroscopic analysis of both components of HM1-8.

Parameters	Primary	Secondary
$v \sin i$ [km s^{-1}]	105 ± 14	82 ± 15
$v_{\rm mac}$ [km s^{-1}]	67 ± 6	22 ± 7
$T_{\rm eff}$ [K]	41200 ± 1200	34500 ± 1200
log g [dex]	3.76 ± 0.15	4.0 (fixed)
log Q [dex]	−12.3 ± 0.1	−13.0 ± 0.3
Fundamental parameters adopting:		
M_V [mag]	-5.2	-3.7
R [R$_\odot$]	11.0 ± 0.2	5.7 ± 0.1
log $(L/L_\odot)$ [dex]	5.49 ± 0.04	4.61 ± 0.04
M_{sp} [M$_\odot$]	26.8 ± 8.2	< 9.7

presented in Table 5, while the comparison between the spectrum and the best FASTWIND model is illustrated in Fig. 6. Again, the agreement between model and spectrum is fairly good.

An important parameter is the flux ratio between components, needed to calculate the dilution factors. As we pointed previously, a flux ratio was estimated from the spectral types and magnitude calibration. To determine the dilution factors, we use the FASTWIND models representing each component of the system (as they were calculated previously), and diluted them by several dilution factors from f_1=0.6-0.9 and f_2=0.1-0.4 for the primary and secondary, respectively. Then, we compared them with an observed spectrum and concluded that f_1=0.8 and f_2=0.2 are proper values.

3.6 Struve-Sahade Effect

During the visual inspection of the spectra, we noticed changes in the relative intensity of the components in the He I λ7065 line at the two quadratures. These spectral variations could be indicative of the presence of the Struve-Sahade (S-S) effect. We understand it as the apparent strengthening (weakening) of some absorption lines of both components when they are approaching (receding); which is different from the traditional concept where the lines associated with the secondary component were the ones that presented changes (see Linder et al. 2007). Since its discovery (Pickering & Bailey 1896), there were attempts to explain this effect without being possible to fully understand it, and with the years it became more likely the idea that there are several mechanisms producing this effect (Bagnuolo et al. 1999; Linder et al. 2007; Palate et al. 2013). In the recent work of Abdul-Masih et al. (2020), they present a model that takes into account the 3-dimensional surface geometry of a system to produce spectral profiles at given phases and orientations, and they could represent this effect in the HD 165052 system. Fig. 7 shows the He I λ7065 line in two FEROS spectra at two opposite quadratures to picture the S-S effect. Also, it is displayed the equivalent width (EW) ratio of He I λ7065/He I λ5876 lines (S-S effect is not observed in He I λ5876), for both components. To check the reliability of the spectral variations, we also measured the EW for the DIB λ5850 in the same spectra finding that it is constant at 5% level, which is much smaller than the change in He I λ7065, thus the equivalent width variations observed in this line are real and not due to noise or normalisation errors. It must be noted, however, that flanking the He I λ7065 line there are three faint DIBs ($\lambda\lambda$7061.0, 7062.5 and 7069.0), which might slightly affect the EW measurements.

4 THE SPECTROSCOPIC ORBIT

As a first step, we verified that the new RV data are compatible with the periodicity reported by Gamen et al. (2008). This period was used as initial input, for the spectroscopic orbit calculation. We then fitted the spectroscopic orbit to the different lines measured (see Table 4) by means of the FOTEL program (acronym for *Fotometric Elements* Hadrava 2004), deriving a RV orbital solution which can be combined with light-curve (LC) analysis of binary systems. The code converged quickly to robust orbital solutions using the different RV datasets listed in Table 4, letting free all the orbital parameters. In particular, the orbital solutions obtained with He I λ5876 and by means of the cross-correlation process using disentangled spectra shown the smallest errors, in special the latter one. Therefore, we consider that the spectroscopic orbit solutions obtained with the RVs determined by means the cross-correlation process as the most representative for this binary system. The parameters derived from this orbital solution are listed in the Table 6.

5 THE ECLIPSING BINARY MODEL

Phasing the photometric observations with the spectroscopic orbital period reveals a small and sharp drop in brightness at a phase close to the lower conjunction (the early-O star in the back side of the orbit). This feature can be understood as the detection of the primary eclipse of the system, i.e. when the secondary star is partially occulting the disk of the primary component, as depicted below in Fig. 9.

Under the assumption of a sharp primary eclipse, we performed a modeling of the photometric time series by means of the FOTEL code. For this basic model, the user provides initial values for the orbital elements (P, T_0, e, ω, $K_{1,2}$), and fixed values for the effective temperature of the stars, limb-darkening coefficients, magnitudes, and radii. Orbital elements were fixed from the spectroscopic solution.

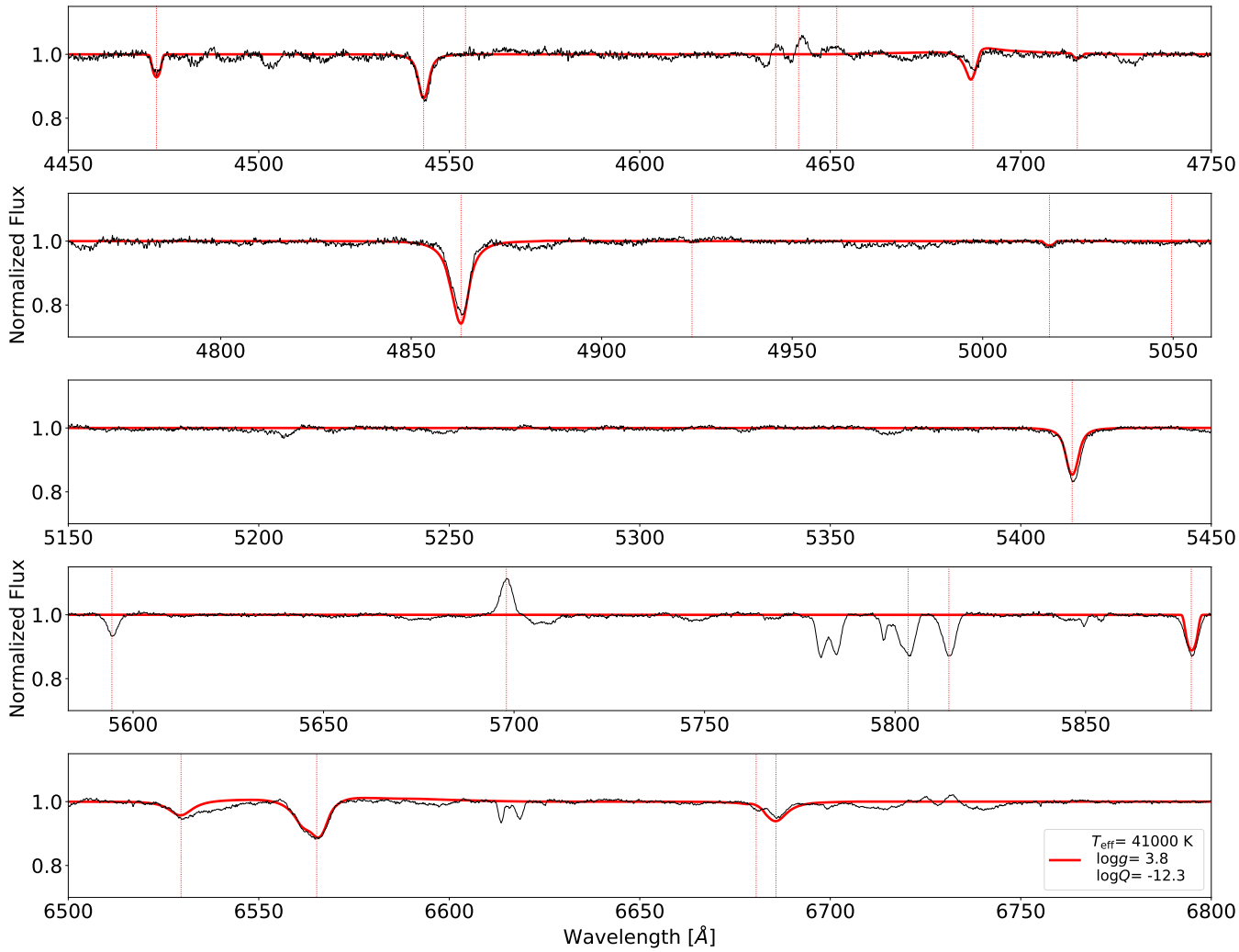

Figure 5. Template of HM1-8a obtained from the disentangling method, compared with a FASTWIND model (parameters in Table 5). In each panel, we draw vertical lines depicting the (shifted) wavelengths of the same spectral features indicated in Fig. 1.

Limb-darkening coefficients were taken from the Castelli & Kurucz (2003) calculations for a linear law, while $T_{\rm eff}$ and log g were adopted from the quantitative analysis performed with the IACOB-GBAT code. Magnitudes in V-band for each component were calculated considering the dilution factors and the apparent magnitude of the system (m_V = 12.52 mag; Reed 2003). As the primary eclipse is grazing partial and no secondary one is detected, some constraints could be taken about radii. The luminosity of each star can be obtained adopting a distance of $d = 2805^{+146}_{-157}$ pc (Bailer-Jones et al. 2021), an extinction in the V-band, $A_V = 5.678 \pm 0.054$ (Maíz Apellániz & Barbá 2018), bolometric corrections, $BC_{\rm a} = -3.67$ mag and $BC_{\rm b} = -2.97$ mag (Martins & Plez 2006), and the calculated dilution factors (actually, the flux ratio). Then, by means of the Stefan-Boltzmann formula, we can infer the radii. Then, we ran FOTEL with three different set of radii (considering a range in luminosity) to determine the inclination of the system. Derived parameters are listed in Table 6, and the light curve model represented in Fig. 8 together to phased photometric observations.

Larger luminosity implies larger radius, and then, smaller orbital inclination in order to keep the depth of the eclipse, and therefore, larger absolute masses. Smaller masses are obtained in the case of smaller luminosities and radii. In this way, we adopt as the error interval of the inclination these calculations made with different radii and luminosities, which is propagated as an estimate in the other orbital parameters that consider the inclination (semi-axes and masses).

In Fig. 9 we provide an illustration of the system's configuration at the inferior ($\Phi = 0.9$) and superior ($\Phi = 0.4$) conjunctions according to our orbital solution[5]. Both stars are represented as seen from the observer. It can be noticed that due to the orbital eccentricity, a grazing primary eclipse is happening near the periastron passage, while the secondary one cannot occur due to larger separation of the stars in the superior conjunction.

For completeness, we also plot the $\log L - \log T_{\rm eff}$ plane in Fig. 10 (where evolutionary tracks and isochrones were calculated with the code described in Benvenuto & De Vito 2003). We have assumed solar abundances with $Z = 0.014$ and moderate overshooting with $\alpha_{\rm OV} = 0.2$. In these calculations we have neglected the effects of

[5] This illustration was obtained with Phoebe-1.0 (Prša & Zwitter 2005) by adopting the parameters in Table 6.

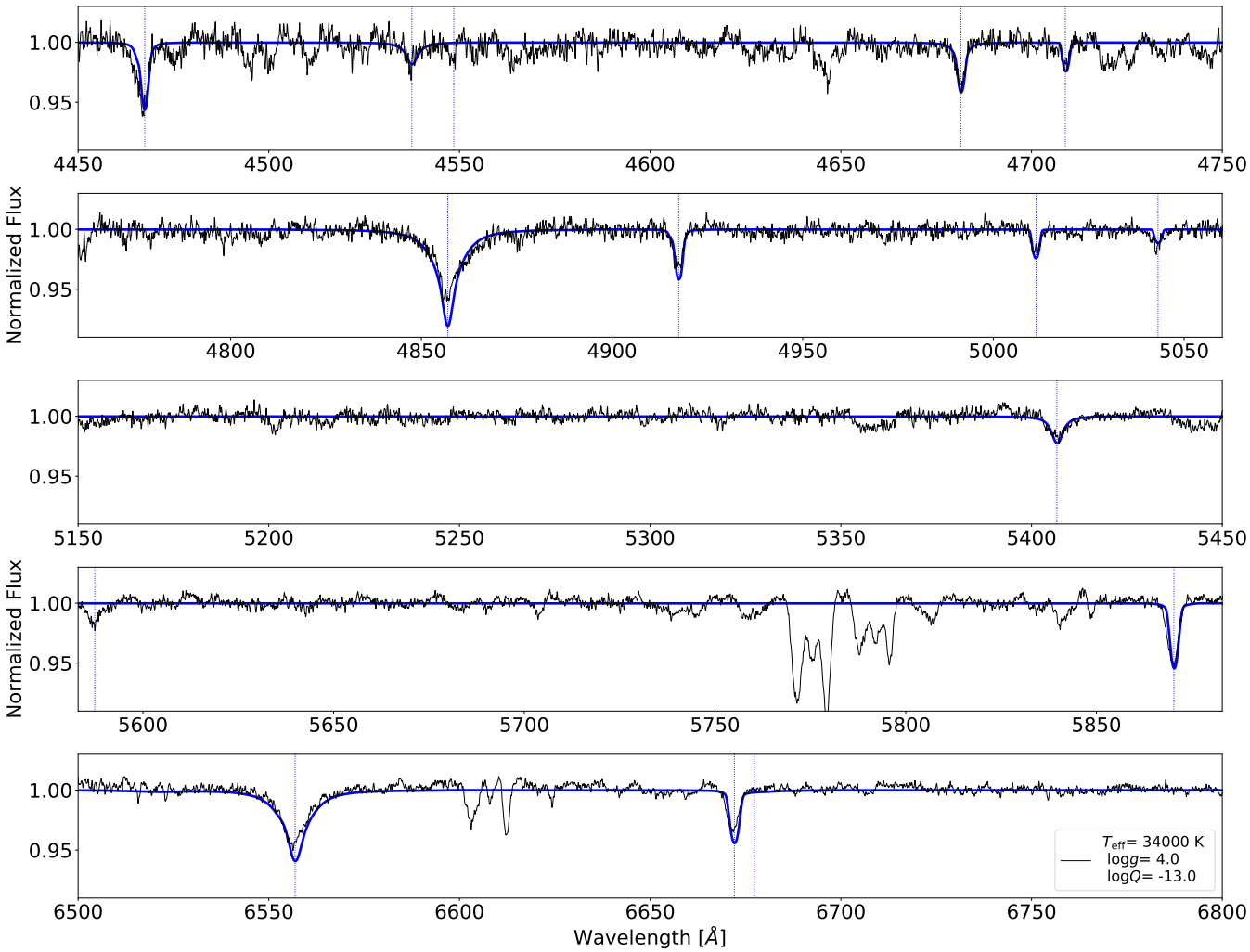

Figure 6. Template of HM1-8b obtained from the disentangling method, compared with a FASTWIND model (parameters in Table 5). In each panel, we draw vertical lines depicting the (shifted) wavelengths of He I λ4471, He II λ4542, Si III λ4553, He II λ4686, He I λ4713, H$_\beta$, He I λ4922, He I λ5016, He I λ5047, He II λ5411, O III λ5592, He I λ5875, He II λ6527, H$_\alpha$, He I λ6678, He II λ6683.

stellar rotation on the evolution of the stars. This approach is fairly good considering that components in the pair rotate far slower than the breakup velocity (see below). Taking into account the values for the masses of the components given in Table 6, and the mass loss rates derived from the models, we deduce that their masses on the ZAMS were about 34^{+3}_{-2}M$_\odot$ and 17.9^{+2}_{-1}M$_\odot$, assuming an age of about 2 Ma for the binary. Tracks for ages up to 4 Ma, corresponding to these masses are shown in Fig. 10 with thick magenta dashed lines. It is important to remark that this system will suffer a Roche lobe overflow at an age of 4.8 Ma. Clearly, the system is younger and the components of the pair are still detached.

6 X-RAY ANALYSIS

In order to characterize the X-ray emission of HM1 8 system and to compare it with the results of Nazé et al. (2013), we performed a spectral analysis to the calibrated and filtered events lists from *XMM-Newton* observations (as explained in Sec. 2.3), where we extracted and fitted a spectrum of each EPIC camera. In particular, we want to determine if the emission is associated with the winds of the stars or a colliding wind region (CWR).

Firstly, we extracted a spectrum of HM1 8 for the EPIC MOS1/2 and pn cameras, following the spectrum extraction threads for EPIC cameras[6], for which we acquired three different images obtained by filtering the event lists by three energy bands: soft (0.5-1.2 keV), medium (1.2-2.5 keV) and hard (2.5-10 keV), and combined them. We chose regions to extract the source+background and the background spectra to obtain the source spectrum. The resultant spectrum was grouped to assure SNR=1 per bin.

Inspecting the images in the 3 energy bands we noticed that, for energies greater than 3 keV, there is no detectable signal from the source that could be distinguished from the background noise, so the spectral analysis was limited to the energy range 0.5-3 keV. In this sense, we avoid possible noise contamination that could hinder the fit of the extracted spectrum. To fit the spectra, we used the XSPEC package (version 12.11.1; Arnaud 1996), choosing an APEC model (an emission spectrum from collisionally-ionized diffuse gas, calculated

[6] https://www.cosmos.esa.int/web/xmm-newton/sas-threads

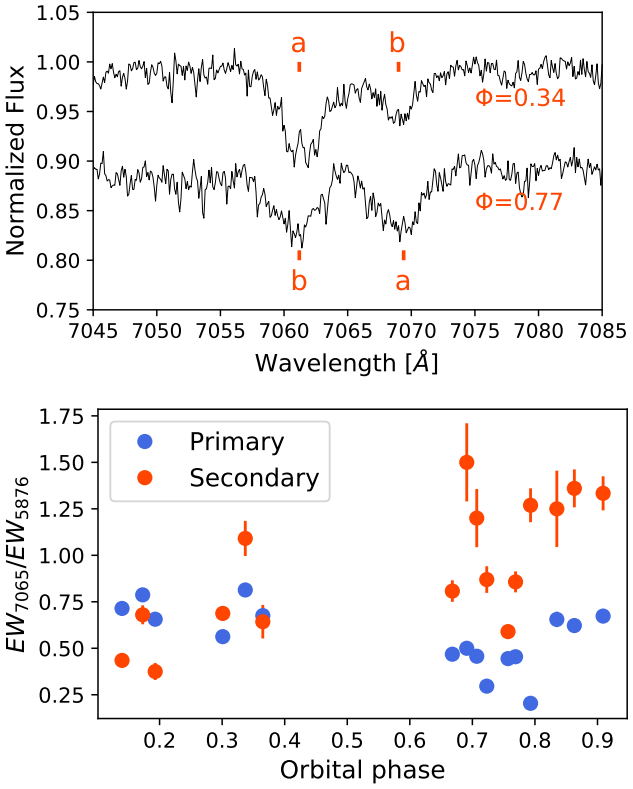

Figure 7. Top: two FEROS spectra around He I λ7065, at different orbital phases (upper one with the secondary component receding and bottom one with the secondary approaching) where the S-S effect can be noticed. Bottom: He I λ7065 to He I λ5876 EW ratio vs orbital phase for both components of HM1 8. It can be seen how the ratio change with the orbital phase, being more evident for the secondary component.

with the AtomDB atomic database[7]), modified by the Tuebingen-Boulder ISM absorption model (TBabs; Wilms et al. 2000), acting on the energy range 0.5-3 keV. Due to the low counts per channel in the spectrum, we used c-statistic to perform the fit; which assumes a Poisson distribution instead of a Gaussian one. Fig. 11 shows the star spectrum for the three cameras and the best fit for each one, and Table 7 presents the fitted parameters. It can be seen that, considering the errors, our results are similar to those obtained by Nazé et al. (2013).

Then, we calculated the quotient L_X/L_{BOL}, which has a typical value of 10^{-7} for the winds of the O-type stars (Nazé et al. 2013; Nebot Gómez-Morán & Oskinova 2018 and references therein). It is assumed that for larger values, the emission comes from the colliding winds region, otherwise it comes from the winds of the components (Sana et al. 2006; Chlebowski 1984, 1989). To get this quotient, we took the bolometric luminosities considered in Sect. 5 and estimated the X-ray luminosity of the system by calculating the flux F_X from the fitted model of the spectrum. We used the FLUX task of XSPEC, which represents the flux in X-rays corrected by ISM absorption, in the range of energy where HM1 8 emits: 0.5-3 keV. From this, we obtained $F_X = 2.31^{+0.11}_{-0.27} \times 10^{-14}$ergs^{-1} cm^{-2}.

Then, taking into account the distance we found the X-ray luminosity $L_X = 2.2^{+0.3}_{-0.5} \times 10^{31}$ erg s^{-1} Finally, we obtained the quotient $L_X/L_{BOL} \approx (0.19^{+0.03}_{-0.04}) \times 10^{-7}$, which would indicate that the radiation comes from the stellar wind of the primary component. This is different of what Nazé et al. (2013) found, probably due to they considered the X-ray flux up to 8 keV and in this work we cut it at 3 keV because HM1 8 has not detectable emission beyond this point.

One may wonder if a colliding winds region actually exists but

[7] http://www.atomdb.org

Table 6. Solution given by FOTEL putting together the RV measurements and the photometric data.

Element	Value		
Spectroscopic orbital solution			
P [d]	5.87820 ± 0.00008		
T_0 [HJD −2 400 000]	$56\,815.30 \pm 0.09$		
e	0.14 ± 0.01		
V_γ^a [km s^{-1}]	-20.2 ± 1.6		
V_γ^b [km s^{-1}]	-11.5 ± 2.8		
ω[°]	119 ± 10		
K_a [km s^{-1}]	143 ± 2		
K_b [km s^{-1}]	273 ± 3		
$q = M_b/M_a$	0.52 ± 0.02		
$a_a \sin i$ [R$_\odot$]	16.4 ± 0.1		
$a_b \sin i$ [R$_\odot$]	31.3 ± 0.4		
$M_a \sin^3 i$ [M$_\odot$]	28.4 ± 0.7		
$M_b \sin^3 i$ [M$_\odot$]	14.6 ± 0.4		
r.m.s$_{(O-C)^a}$ [km s^{-1}]	4.5		
r.m.s$_{(O-C)^b}$ [km s^{-1}]	5.8		
Fixed parameters			
V_a [mag]	12.8		
V_b [mag]	14.3		
T_{eff}^a [K]	41 200		
T_{eff}^b [K]	34 500		
M_{Va} [mag]	-5.4	-5.2	-5.0
M_{Vb} [mag]	-3.9	-3.7	-3.5
R_a [R$_\odot$]	11.6	10.8	9.6
R_b [R$_\odot$]	6.2	5.8	5.1
Derived parameters			
i [°]	68.0	70.0	72.0
a [R$_\odot$]	51.6	50.7	50.3
M_a [M$_\odot$]	35.0	33.6	32.4
M_b [M$_\odot$]	18.2	17.7	17.0
r.m.s$_{(O-C)\ photometry}$ [mag]		0.013	

Table 7. Parameters derived from the fitted with XSPEC using model c*TBabs*apec. Nazé et al. (2013) model: wabs*wabs*apec; where the first wabs was fixed with $N_H = 1.1 \times 10^{22}$ cm^{-2}. In both works a solar abundance was adopted. The normalisation of the apec model is given as $10^{-14} \int n_e n_H dV/d^2$, where d is the distance to the source (in cm), n_e and n_H are the electron and hydrogen densities of the source (in cm^{-3}). Since counts of the *pn* camera are greater than the MOS cameras, we fixed $c_{pn} = 1.0$ and obtained the others with respect to this.

Parameter	This work	Nazé et al. (2013)
N_H [10^{22} cm^{-2}]	1.97 ± 0.2	$1.1 + (0.4 \pm 0.08)$
kT [keV]	$0.75^{+0.12}_{-0.11}$	0.93 ± 0.07
norm [10^{-4} cm^{-5}]	$1.65^{+0.65}_{-0.42}$	1.8 ± 0.2
c_{MOS1}	0.99 ± 0.2	-
c_{MOS2}	0.98 ± 0.2	-
Reduced χ^2	0.95	1.12

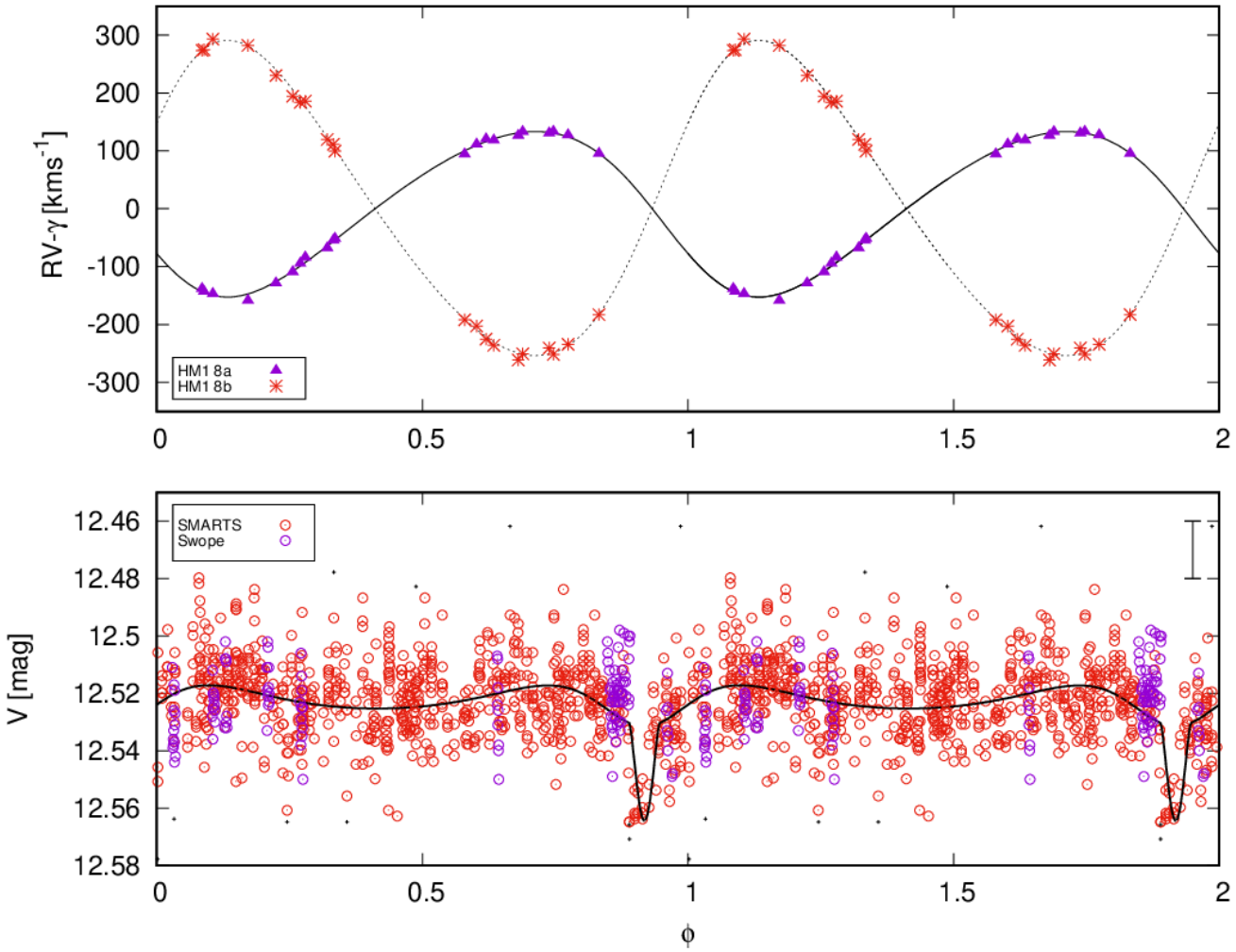

Figure 8. Upper panel: RV curve of HM1 8 obtained through cross-correlation method and phased using the ephemeris from Table 6. The systemic velocities determined for each component was subtracted. Solid line and triangles: primary component; dotted line and crosses: secondary component. RV error bars are smaller than the symbols. Lower panel: light curve in V filter, phased with the same period. Red points: SMARTS Yale 1-m telescope; purple: Swope telescope. Small dots: data not considered in the solution (3σ clipping). Solid line: FOTEL model. Error bar represents a typical photometric error.

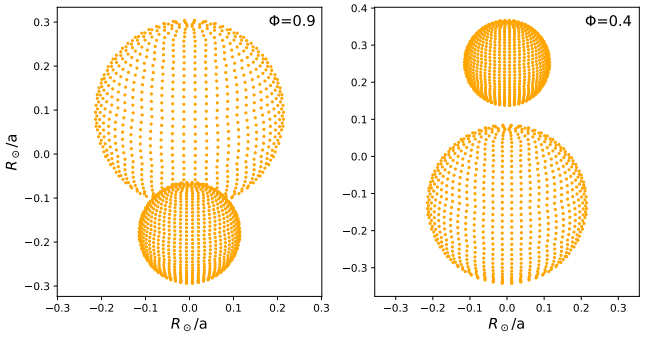

Figure 9. FOTEL model configuration of the binary system HM1 8 projected in the plane of the sky during the conjunction phases.

was not visible at the time of the X-ray observation so, to discard it, we made a scheme of the stars positions during the *XMM-Newton* observation. As can be seen in Figure 12, if a colliding winds region exists, it should be detected since this region shall be very close to the surface of the secondary component, which was visible during the observation. Moreover, we do not see in the optical spectra indications of a possible colliding winds influence in the H_α line since it is in absorption in all the spectra.

7 TIDAL EVOLUTION OF THE PAIR

We now study the tidal evolution of HM1 8 with the intention of comparing the results of the models with the observed state of the system. In particular, since an orbital eccentricity was found from the observational analysis[8], it is interesting to compute the circularisation timescale and compare it with the age of the system.

In order to compute the tidal evolution of the pair we need to solve a system of six ordinary, non linear differential equations. These

[8] This is a clear indication that the system has not suffered a Roche Lobe overflow (RLOF) yet and the pair is in a detached configuration. If the system were in the RLOF state, the orbit would be almost circular

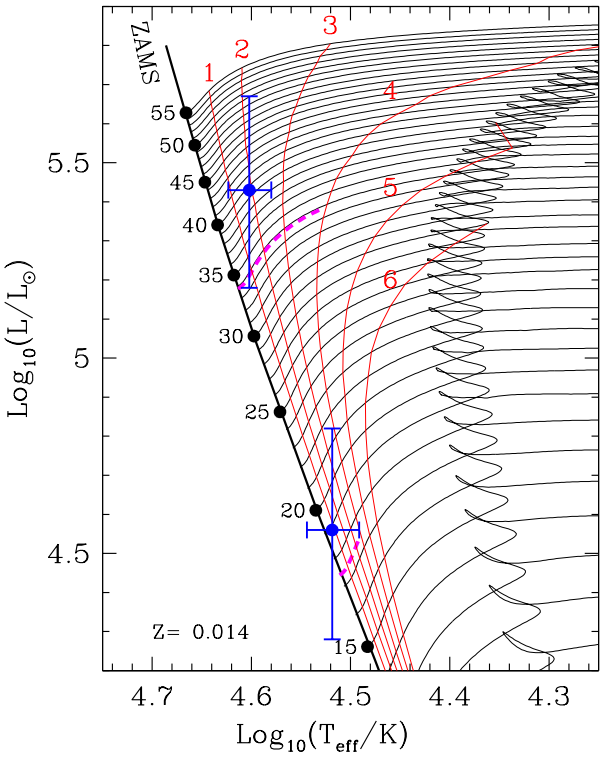

Figure 10. $\log L - \log T_{\rm eff}$ diagram. Black lines represent the evolutionary tracks for solar composition single stars from 11 $M_\odot$ to 55 $M_\odot$. Thin red lines denote isochrones every 1 Ma. Thick dashed magenta lines indicate the evolution of stars with the masses presented in Table 6 up to an age of 4 Ma. The error bars corresponding to the luminosity and effective temperature of each component, given in Table 5 are denoted in blue. These evolutionary tracks were calculated employing the code described in Benvenuto & De Vito (2003).

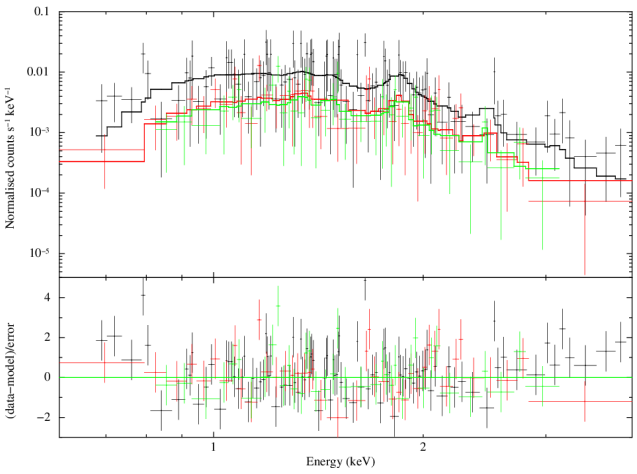

Figure 11. X-ray spectrum of HM1 8 for the three EPIC cameras with the fitted c*TBabs*APEC model. Black: *pn* camera; red: MOS1 camera; green: MOS2 camera. The upper panel shows normalised counts vs. energy, and the lower panel represents the residuals.

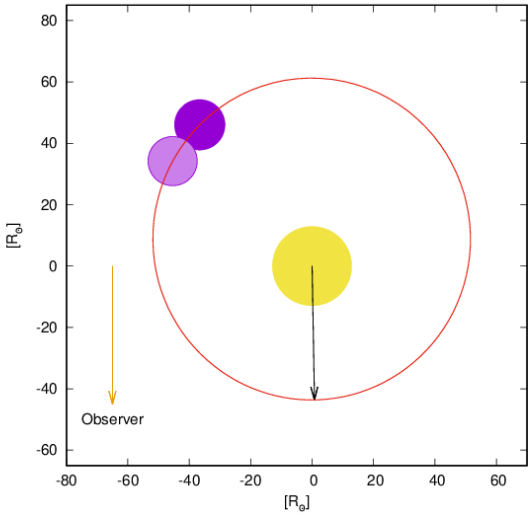

Figure 12. Configuration of the HM1 8 binary system during the X-ray observation of March 10, 2010. Yellow filled circle: primary component. Dark (light) purple filled circle: secondary component position at the start (end) of X-ray observation. Red ellipse: relative orbit of the secondary component. Orange arrow: direction to the observer. Black arrow: periastron position of the relative orbit.

correspond to the evolution of the major semiaxis of the orbit a (or, equivalently, the orbital period $P_{\rm orb}$), the eccentricity e, the angular rotation $\omega_{\rm i}$ of each component and the inclination of their rotational axes $i_{\rm i}$ with respect to the orbital plane.

The tidal equations we solve are given by Repetto & Nelemans (2014) that are a generalization of those given by Hut (1981) (see also Belczynski et al. 2008). These equations have been solved by a fully implicit, finite differences algorithm suitable for problems that may reach an equilibrium situation.

We assumed that the initial masses of the components were of $33.8 M_\odot$ and $17.9 M_\odot$. If we assume an age of 2 Ma, these masses on the ZAMS evolve to the observed values. As stated above, we assumed solar composition, moderate overshooting and neglected the effects of rotation on the evolution of the components. Nevertheless, stellar rotation is considered in the tidal evolution.

This treatment cannot be considered as contradictory: Rotation of the components is far slower than critical rotation (and so, internal mixing due to rotation has a minor effect). On the contrary, considering the exchange between the angular momentum contained in the rotation of the components and the orbit is essential for a correct treatment of the tidal evolution.

In order to solve the tidal evolution equations we need to know the evolution of some important quantities of each component of the pair. These are the masses, radii, and radii of gyration k of the components ($I = k^2 M R^2$, where I is the moment of inertia of the star). They have been computed with the stellar code presented in Benvenuto & De Vito (2003) and the results are presented in Fig. 13. Since these are smooth functions, we tabulated them in advance, neglecting the effects of tides on the evolution of this pair. This is a natural approximation, since HM1 8 is still a well detached pair.

To explore the tidal evolution of the pair, we shall consider three different situations by assuming different initial conditions. Cases I, II, and III are defined in order to analyse the sensitivity of the tidal evolution of the binary system under variations of the initial orbital period, eccentricity and angular velocity of rotation of the primary.

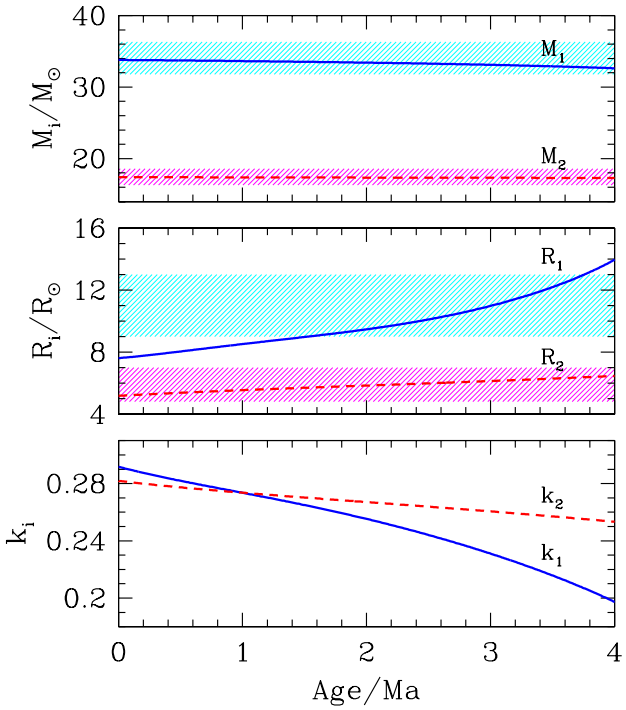

Figure 13. Evolution of the masses (upper panel), radii (middle panel) with their corresponding uncertainties. In the lower panel we present the radii of gyration for the components of HM1 8.

We also tested the variation of the tidal evolution by changing the inclination of the axis of rotation of the components, as well as by changing the angular velocity of the secondary component. As these variations have a small impact on the tidal evolution of the pair we shall restrict ourselves to the discussion of the results corresponding to cases I, II, and III.

We define $\varpi_i = (\omega_i)_{\rm init}/(\omega_i)_{\rm cr}$, where $(\omega_i^2)_{\rm cr} = GM_i/R_i^3$ is the critical rotation rate if the star is spherical. It may be adequate to remark that here we employ $(\omega_i)_{\rm cr}$ only to gauge the relevance of rotation on the structure. Considering that the components of HM1 8 have projected tangential velocities of rotation of the order of 100 km s^{-1} and the values presented in Fig. 13 for the masses and radii, we find that $\varpi_i \approx 1/7$ which, as discussed above, justifies the employment of evolutionary tracks of non rotating models.

- Case I: Consider $(e)_{\rm init} = 0.29$; $\varpi_1 = 0.20$; $(i_1)_{\rm init} = 1.0$; $\varpi_2 = 0.20$; $(i_2)_{\rm init} = 1.0$ and vary the orbital period: $(P_{\rm orb})_{\rm init}$ = 5.705, 5.848, 5.994, 6.144, and 6.297 days.
- Case II: Consider $(P_{\rm orb})_{\rm init} = 6.000$ days; $\varpi_1 = 0.20$; $(i_1)_{\rm init} = 1.0$; $\varpi_2 = 0.20$; $(i_2)_{\rm init} = 1.0$ and vary the eccentricity $(e)_{\rm init} = 0.20$, 0.220, 0.242, 0.266, and 0.293.
- Case III: Consider $(P_{\rm orb})_{\rm init} = 5.900$ days; $(e)_{\rm init} = 0.20$; $(i_1)_{\rm init} = 1.0$; $\varpi_2 = 0.20$; $(i_2)_{\rm init} = 1.0$ and vary the angular velocity of the primary $\varpi_1 = 0.100$, 0.150, 0.225, 0.337, and 0.506.

The main results of these simulations are shown in Fig. 14. From these results we find that if the initial eccentricity of the pair was larger than the one now observed, there is a clear tendency of the system to circularisation and the timescale to reach the observed value is of the order of two to four million years, comparable to the evolutionary timescale of the primary component of the pair (see upper panel of Fig. 14). This also tell us that, as the system is not yet circularised, consistent with an age less than 4 Ma. In the lower panel of Fig. 14 we show the evolution of the orbital period of the pair. It changes on a narrow interval, since the binary components are at a relative distance appreciably larger than their respective sizes. As a result, the exchange of angular momentum between components is rather weak.

For completeness, in Fig. 15 we present the tidal evolution of a system with the masses observed in HM1 8 that at an age of 2 Ma is in agreement with of observations. This corresponds for a particular set of initial conditions. In fact there should be a set of infinitely degenerate initial conditions that would also give compatibility with observations. While it is not the goal of this section to perform an exploration of these conditions, the chosen example proves that it is possible to get a nice agreement between the standard tidal evolution theory and our observations.

8 SUMMARY AND CONCLUSIONS

Using optical photometric and spectroscopic data, and X-ray observations, a comprehensive study of the massive binary system HM1 8 was performed. This analysis includes the computation of an improved orbital solution, updated spectral classifications of both stellar components, and the determination of the fundamental parameters of the system. The tidal evolution of the binary was also modelled.

A spectral disentangling method applied to the observed composite spectra lead to the individual spectrum of each component, over which RV and quantitative spectral analyses were performed.

The binary star HM1 8 is a very massive eclipsing system whose components, classified as O4.5 IV and O9.7 V, are characterized by a period of P=5.8782 days.

The orbital period we obtained is very close to the value reported by Gamen et al. (2008). We were able to fit a spectroscopic orbital solution that indicates an eccentric orbit (e=0.14) with its major axis pointing very close to our line of sight. The fitted mass ratio $q \sim 0.5$ is the most common value in massive binary systems according to Barbá et al. (2017).

We detected a decrease in brightness synchronised with the phase of conjunction, according to the spectroscopic orbital solution, which corresponds to a partial eclipse of the primary star from the secondary one and allowed us to obtain the inclination of the system (i=70°) and, with it, the absolute masses of the components (M_a=33.6 $M_\odot$ and M_b=17.7 $M_\odot$).

It is common knowledge the importance of determining reliable masses, and how poorly known they are for early-type stars, therein lies the relevance of the determination of a Galactic O4.5 IV mass by the method of eclipsing binaries. Before this work, the earliest giant star with a known mass (also obtained by the eclipsing binaries method) was HD152248b, an O7 III star with $M = 30.1 \pm 0.4$ $M_\odot$ (Mayer et al. 2008), and the earliest subgiant was HD152218a, an O9 IV, with $M = 19.8 \pm 1.5$ $M_\odot$ (Rauw et al. 2016). For the secondary, the dynamical mass we obtained is $M_2 \approx 18$ $M_\odot$; and the other Galactic O9.7 V star mass, calculated with the eclipsing binary method, is HD152218b (Rauw et al. 2016) with $M = 15.0 \pm 1.1$ $M_\odot$.

We also performed a new X-ray spectroscopic analysis of the *XMM-Newton* data and obtained plasma parameters similar to those from Nazé et al. (2013). Comparing the X-ray flux with the bolo-

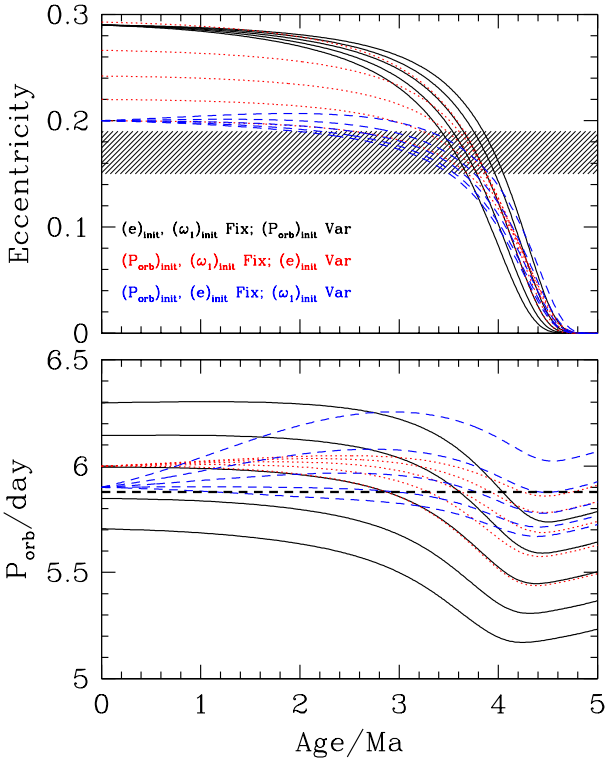

Figure 14. Tidal evolution of the HM1 8 system according to the models described in this paper. The upper and lower panels depict the time evolution of the system eccentricity and period, respectively. Black solid curves represent case I: time evolution for 5 different values of the initial orbital period. The upper curve corresponds to the larger $P_{\rm orb,init}$ for which the orbital period and the eccentricity show the slower evolution with time. Red dotted lines represent Case II: time evolution for 5 different values of the initial eccentricity. The upper curve corresponds to the larger $(e)_{\rm init}$ for which the changes in e and P with evolution are also slower. Blue dashed lines represent Case III: time evolution of the system for 5 different values of the primary rotational velocity. Again, the upper curve corresponds to the larger $\varpi_{1,\rm init}$ for which the period and eccentricity show the slower evolution. In the upper panel, tilted dashed lines indicate the range of eccentricities compatible with observations. In the lower panel, the period is denoted with a horizontal dashed line.

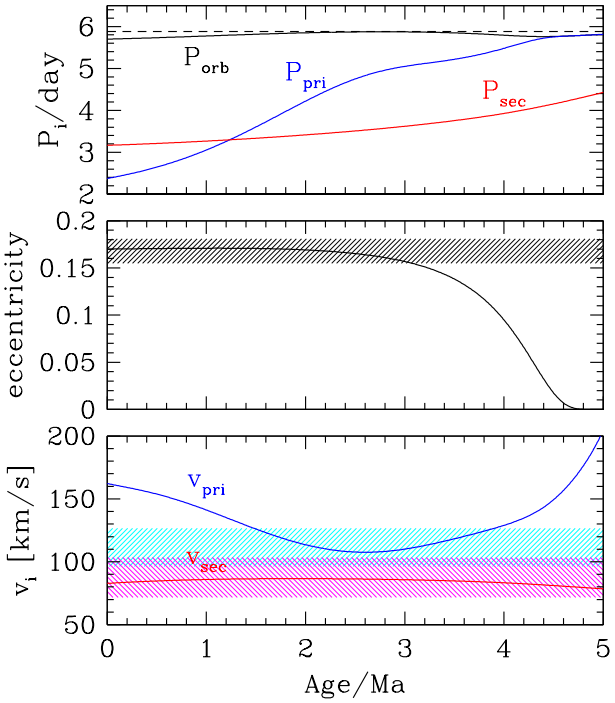

Figure 15. Evolution of the periods of the orbit and of rotation of each component, eccentricity of the orbit, and rotational velocities of a system with the masses corresponding to the case of HM1 8. Here we assumed $(P_{\rm orb})_{\rm init}$ = 5.70 days,$(P_{\rm pri})_{\rm init}$ = 2.37 days,$(P_{\rm sec})_{\rm init}$ = 3.17 days, $(e)_{\rm init}$ = 0.17; $(i_1)_{\rm init}$ = $(i_2)_{\rm init}$ = 0.0. For this particular configuration we find that at the age of 2 Ma this configuration is in agreement with the orbital period (represented with a dashed line in the upper panel), eccentricity and rotational velocities. In the lower panel the cyan (magenta) shaded region represents the uncertainty in the rotational velocity for the primary (secondary) component of the pair. Notice that the primary is synchronized to the orbit in ≈ 4 Ma while the secondary does not reach this state in 5 Ma of evolution.

metric luminosity we estimated that the X-ray emission of HM1 8 originates in the primary wind and that there is not a colliding winds region.

We studied the tidal evolution of the binary system by solving the equations of Repetto & Nelemans (2014). As circularisation occurs on a timescale of 4 Ma and the expected age of the system is shorter, this provides a description consistent with the eccentric solution of the orbit deduced from observations. Furthermore, the evolution of the period shows slight changes along time, which correspond to a weak exchange of angular momentum, as expected for a binary system in which the distance between the components is appreciably larger than their sizes.

At last, we shall give some context to this study of the HM1 8 system. First, it is important though not very common to obtain absolute dynamical masses of stars, in general due to the lack of information about orbital inclinations. In this case, it takes another level of importance since we have two massive components; furthermore, one of them is an O4.5 IV star which is the earliest subgiant star with a known dynamical mass. Finally, it is notable that all the different techniques we used to analyse this system gave us consistent results; therefore we have a comprehensive view of the fundamental parameters, the behaviour and the evolution of this massive binary system.

ACKNOWLEDGEMENTS

The authors warmly thank the referee, Ian Howarth, for his detailed review, suggestions and guidance that helped improving the manuscript. We thank the directors and staff at LCO, CTIO and La Silla for the use of their facilities and their kind hospitality during the observing runs. C.N.R. acknowledges support from Consejo Nacional de Investigaciones Científicas y Técnicas (CONICET) through the Beca Interna Doctoral grant and from Asociación Argentina de

Astronomía through the Beca de Estímulo a las Vocaciones Científicas grant. C.N.R., G.A.F., and R.G. acknowledge support from grant PICT 2019-0344. R.H.B. acknowledges support from ANID FONDECYT Regular Project No. 1211903. We thank Sergio Simón-Díaz for his valuable help with the IACOB tools. This work was based on observations obtained with *XMM-Newton*, an ESA science mission with instruments and contributions directly funded by ESA Member States and NASA. This research has made use of the NASA's Astrophysics Data System and the SIMBAD database, operated at CDS, Strasbourg, France.

DATA AVAILABILITY

The optical spectroscopic data underlying this article belongs to the *OWN Survey* team and will be shared on reasonable request to Dr. Rodolfo H. Barba; while the optical photometric data are available in the article and in its online supplementary material. Finally, the X-ray data underlying this article are available in the *XMM-Newton* Science Archive at `http://nxsa.esac.esa.int/nxsa-web/#search`, and can be accessed with the observation ID 0600080101.

REFERENCES

Abdul-Masih M., Sana H., Conroy K. E., Sundqvist J., Prša A., Kochoska A., Puls J., 2020, A&A, 636, A59
Arnaud K. A., 1996, in Jacoby G. H., Barnes J., eds, Astronomical Society of the Pacific Conference Series Vol. 101, Astronomical Data Analysis Software and Systems V. p. 17
Bagnuolo William G. J., Gies D. R., Riddle R., Penny L. R., 1999, ApJ, 527, 353
Bailer-Jones C. A. L., Rybizki J., Fouesneau M., Demleitner M., Andrae R., 2021, AJ, 161, 147
Barbá R. H., Gamen R., Arias J. I., Morrell N. I., 2017, in Eldridge J. J., Bray J. C., McClelland L. A. S., Xiao L., eds, IAU Symposium Vol. 329, The Lives and Death-Throes of Massive Stars. pp 89–96, doi:10.1017/S1743921317003258
Barbá R. H., et al., 2020, MNRAS, 494, 3937
Belczynski K., Kalogera V., Rasio F. A., Taam R. E., Zezas A., Bulik T., Maccarone T. J., Ivanova N., 2008, ApJS, 174, 223
Benvenuto O. G., De Vito M. A., 2003, MNRAS, 342, 50
Castelli F., Kurucz R. L., 2003, in Piskunov N., Weiss W. W., Gray D. F., eds, IAU Symposium Vol. 210, Modelling of Stellar Atmospheres. p. A20 (`arXiv:astro-ph/0405087`)
Chiosi C., Maeder A., 1986, ARA&A, 24, 329
Chlebowski T., 1984, Acta Astron., 34, 191
Chlebowski T., 1989, ApJ, 342, 1091
Feldmeier A., Puls J., Pauldrach A. W. A., 1997, A&A, 322, 878
Gamen R., Barbá R. H., Morrell N. I., Arias J., Maíz Apellániz J., 2008, in Revista Mexicana de Astronomia y Astrofisica Conference Series. pp 54–54
González J. F., Levato H., 2006, A&A, 448, 283
Hadrava P., 2004, Publications of the Astronomical Institute of the Czechoslovak Academy of Sciences, 92, 1
Harnden F. R. J., Golub L., Rosner R., Seward F., Topka K., Vaiana G. S., 1979, in Bulletin of the American Astronomical Society. p. 775
Havlen R. J., Moffat A. F. J., 1977, A&A, 58, 351
Hut P., 1981, A&A, 99, 126
Kramida A., Yu. Ralchenko Reader J., and NIST ASD Team 2020, NIST Atomic Spectra Database (ver. 5.8), [Online]. Available: `https://physics.nist.gov/asd` [2021, August 20]. National Institute of Standards and Technology, Gaithersburg, MD.
Langer N., 2012, ARA&A, 50, 107
Linder N., Rauw G., Sana H., De Becker M., Gosset E., 2007, A&A, 474, 193
Lucy L. B., White R. L., 1980, ApJ, 241, 300
Maeder A., 1998, in Friedli D., Edmunds M., Robert C., Drissen L., eds, Astronomical Society of the Pacific Conference Series Vol. 147, Abundance Profiles: Diagnostic Tools for Galaxy History. p. 224
Mahy L., Rauw G., De Becker M., Eenens P., Flores C. A., 2013, A&A, 550, A27
Maíz Apellániz J., Barbá R. H., 2018, A&A, 613, A9
Maíz Apellániz J., et al., 2016, ApJS, 224, 4
Martins F., Plez B., 2006, A&A, 457, 637
Martins F., Schaerer D., Hillier D. J., 2005, A&A, 436, 1049
Massey P., 2003, ARA&A, 41, 15
Massey P., DeGioia-Eastwood K., Waterhouse E., 2001, AJ, 121, 1050
Massey P., Morrell N. I., Neugent K. F., Penny L. R., DeGioia-Eastwood K., Gies D. R., 2012, ApJ, 748, 96
Mayer P., Harmanec P., Nesslinger S., Lorenz R., Drechsel H., Morrell N., Wolf M., 2008, A&A, 481, 183
Nazé Y., Rauw G., Sana H., Corcoran M. F., 2013, A&A, 555, A83
Nebot Gómez-Morán A., Oskinova L. M., 2018, A&A, 620, A89
Owocki S. P., Poe C. H., Castor J. I., 1988, in Bulletin of the American Astronomical Society. p. 1013
Owocki S. P., Sundqvist J. O., Cohen D. H., Gayley K. G., 2013, MNRAS, 429, 3379
Palate M., Rauw G., Koenigsberger G., Moreno E., 2013, A&A, 552, A39
Pickering E. C., Bailey S. I., 1896, ApJ, 4, 235
Prša A., Zwitter T., 2005, ApJ, 628, 426
Puls J., Urbaneja M. A., Venero R., Repolust T., Springmann U., Jokuthy A., Mokiem M. R., 2005, A&A, 435, 669
Rauw G., Rosu S., Noels A., Mahy L., Schmitt J. H. M. M., Godart M., Dupret M. A., Gosset E., 2016, A&A, 594, A33
Reed B. C., 2003, AJ, 125, 2531
Repetto S., Nelemans G., 2014, MNRAS, 444, 542
Sana H., Evans C. J., 2010, Proceedings of the International Astronomical Union, 6, 474
Sana H., Rauw G., Nazé Y., Gosset E., Vreux J. M., 2006, MNRAS, 372, 661
Sana H., et al., 2012, Science, 337, 444
Santolaya-Rey A. E., Puls J., Herrero A., 1997, A&A, 323, 488
Sciortino S., Vaiana G. S., Harnden F. R. J., Ramella M., Morossi C., Rosner R., Schmitt J. H. M. M., 1990, ApJ, 361, 621
Simón-Díaz S., Herrero A., 2007, A&A, 468, 1063
Simón-Díaz S., Herrero A., 2014, A&A, 562, A135
Simón-Díaz S., Castro N., Herrero A., Puls J., Garcia M., Sabín-Sanjulián C., 2011, Journal of Physics: Conference Series, 328, 012021
Simón-Díaz S., Godart M., Castro N., Herrero A., Aerts C., Puls J., Telting J., Grassitelli L., 2017, A&A, 597, A22
Sota A., Maíz Apellániz J., Walborn N. R., Alfaro E. J., Barbá R. H., Morrell N. I., Gamen R. C., Arias J. I., 2011, ApJS, 193, 24
Sota A., Maíz Apellániz J., Morrell N. I., Barbá R. H., Walborn N. R., Gamen R. C., Arias J. I., Alfaro E. J., 2014, ApJS, 211, 10
Striganov A. R., Sventitskii N. S., 1968, Tables of Spectral Lines of Neutral and Ionized Atoms. Springer US, doi:10.1007/978-1-4757-6610-3
Strueder L., et al., 2000, in Truemper J. E., Aschenbach B., eds, Society of Photo-Optical Instrumentation Engineers (SPIE) Conference Series Vol. 4012, X-Ray Optics, Instruments, and Missions III. pp 342–352, doi:10.1117/12.391614
Turner M. J. L., et al., 2001, A&A, 365, L27
Vázquez R. A., Baume G., 2001, A&A, 371, 908
Wilms J., Allen A., McCray R., 2000, ApJ, 542, 914
Zinnecker H., Yorke H. W., 2007, ARA&A, 45, 481

This paper has been typeset from a TEX/LATEX file prepared by the author.